

Three-dimensional simulations of RF wave propagation and power coupling in cold magnetized plasma near an ICRF antenna

Lei-Yu Zhang(张雷宇), Yi-Xuan Li(李屹轩), and Quan-Zhi Zhang(张权治)

Citation: Chin. Phys. B, 2025, 34 (**2**): 025204. DOI: 10.1088/1674-1056/ad9a9c
Journal homepage: http://cpb.iphy.ac.cn; http://iopscience.iop.org/cpb

What follows is a list of articles you may be interested in

Characteristics of the electromagnetic wave propagation in magnetized plasma sheath and practical method for blackout mitigation

Xiang Wu(吴翔), Jiahui Zhang(张珈珲), Guoxiang Dong(董果香), and Lei Shi(石磊)
Chin. Phys. B, 2024, 33 (**5**): 055201. DOI: 10.1088/1674-1056/ad24d4

Propagation of terahertz waves in nonuniform plasma slab under "electromagnetic window"

Hao Li(李郝), Zheng-Ping Zhang(张正平), and Xin Yang (杨鑫)
Chin. Phys. B, 2022, 31 (**3**): 035202. DOI: 10.1088/1674-1056/ac1b90

ISSDE: A Monte Carlo implicit simulation code based on Stratonovich SDE approach of Coulomb collision

Yifeng Zheng(郑艺峰), Jianyuan Xiao(肖建元), Yanpeng Wang(王彦鹏), Jiangshan Zheng(郑江山), and Ge Zhuang(庄革)
Chin. Phys. B, 2021, 30 (**9**): 095201. DOI: 10.1088/1674-1056/abefc7

Energy behavior of Boris algorithm

Abdullah Zafar and Majid Khan
Chin. Phys. B, 2021, 30 (**5**): 055203. DOI: 10.1088/1674-1056/abd161

Damped electrostatic ion acoustic solitary wave structures in quantum plasmas with Bohm potential and spin effects

S Hussain, H Hasnain, Mahnaz Q. Haseeb
Chin. Phys. B, 2019, 28 (**1**): 015202. DOI: 10.1088/1674-1056/28/1/015202

Three-dimensional simulations of RF wave propagation and power coupling in cold magnetized plasma near an ICRF antenna

Lei-Yu Zhang(张雷宇), Yi-Xuan Li(李屹轩), and Quan-Zhi Zhang(张权治)†

School of Physics, Dalian University of Technology, Dalian 116024, *China*

(Received 29 October 2024; revised manuscript received 2 December 2024; accepted manuscript online 5 December 2024)

The electromagnetic wave propagations and their coupling characteristics in magnetized plasma near the antenna of ion cyclotron range of frequencies (ICRF) is studied based on self-developed 3DFEM-IA code. This code effectively resolves the three-dimensional (3D) geometry and the electromagnetic field using the finite element method. Our findings reveal that the distributions of electromagnetic fields and energy flow density significantly depend on the antenna phases, surface current density on the antenna straps, and background plasma density. Notably, the non-uniform surface current density on the antenna straps, resulting from the presence of induced currents, contributes to a reduction in coupling power within the edge plasma. Furthermore, the calculated coupling impedance increases with plasma density, corroborating well with experimental measurements.

Keywords: magnetized plasma, antenna of ion cyclotron range of frequencies (ICRF), power coupling

PACS: 52.25.Xz, 52.40.Fd, 52.50.Qt, 52.65.–y

DOI: 10.1088/1674-1056/ad9a9c **CSTR:** 32038.14.CPB.ad9a9c

1. Introduction

Controlled nuclear fusion is a promising solution for the next generation of clean energy, with the tokamak as one of the most viable paths for achieving this goal. Ion cyclotron range of frequency (ICRF) heating is an auxiliary heating method used in tokamaks, primarily aimed at heating the plasma within a fusion device to achieve ignition conditions. Additionally, ICRF waves can assist in driving the plasma current, thereby contributing to the steady-state operation of the tokamak.[1,2] The ICRF antenna is a critical component of the radio frequency (RF) heating system, responsible for processing and delivering high power to the plasma. To achieve efficient powerful energy injection in a tokamak, enhancing the coupling efficiency of ICRF[3–5] is a crucial area of investigation. This necessitates a comprehensive investigation of RF wave propagation and coupling processes within the edge plasma region adjacent to an antenna.

In prior investigations, the Princeton Plasma Physics Laboratory employed the RANT3D code[6] to examine the influences of the three-dimensional (3D) antenna structure and phase. The research findings demonstrated consistency with the measured loading data of the Tokamak Fusion Test Reactor Bay-M antenna, and calculated specific heat flux on the bumper limiters at various antenna phase. The results indicated that monopole phasing produces significantly higher heat flux than dipole phasing. Milanesio *et al.*[7] utilized the TOPICA code to conduct RF simulations of the antenna with a detailed geometric representation, including the cavity surrounding the port plug and the port extension. They highlighted that the presence of the antenna plug and port cavity significantly affects the field distribution in front of the antenna, particularly around the cavity resonance frequency. Jacquot *et al.*[8] used the commercial software COMSOL to address the incompatibility issue of simultaneously adapting forward (FW) and backward (slow-wave SW) propagating waves within the perfectly matched layer (PML) by assuming a non-uniform density distribution. The inhomogeneous density profile reflects the SW before it reaches the PML. Subsequently, Usoltceva *et al.*[9] introduced a 3D model called RAPLICASOL, which, for the first time, integrated a comprehensive real density distribution into the ICRF antenna model. This innovative approach enables the simultaneous simulation of fast wave and slow wave propagation and absorption, thereby providing a more accurate representation of the ICRF antenna fields compared to models that deliberately exclude slow wave propagation. In addition, comparative validation against the TOPICA code demonstrated that parameters such as coupling impedance and reflection coefficient exhibited high consistency when utilizing the same antenna geometric configuration.[10] Additionally, Qin *et al.*[11] employed the HFSS code to simulate the ICRF antennas of two EAST windows. Their findings revealed that as the number of antenna straps increased, the power spectral peak became narrower, the peak height rose, and all secondary lobes were suppressed, leading to the increase in the driving current. Furthermore, they analyzed the variations in the parallel RF electric field and sheath potential under different antenna phases. Yang *et al.*[12] employed CST software for simulations and concluded that the folded antenna in EAST exhibits a stronger radiative capacity compared to the dual-loop antenna. How-

†Corresponding author. E-mail: qzzhang@dlut.edu.cn

© 2025 Chinese Physical Society and IOP Publishing Ltd. All rights, including for text and data mining, AI training, and similar technologies, are reserved.

ever, the folded antenna also generates a higher RF potential on the adjacent limiter, which diminishes its effectiveness relative to the dual-loop antenna concerning impurity release and antenna breakdown.

Although numerous studies have laid important theoretical foundations and practical experiences for the design and optimization of ICRF antennas, several critical issues remain insufficiently addressed. For instance, the impact of induced currents, commonly generated on the surfaces of various components within antenna systems, on the propagation of electromagnetic fields and energy flow density vectors remain significantly underexplored. Moreover, the power coupling characteristics under complex operating conditions (such as various antenna phases, plasma density profiles, surface current density distributions) lack a systematic theoretical study.

In this study, the simulation employed a self-developed "3DFEM-IA" code based on Matlab platform, utilizing the finite element method, which enables the resolution of the 3D geometric structure of the antenna system while simultaneously calculating the electromagnetic field and the power coupling characteristics in a self-consistent manner. The simulation examined the electromagnetic field propagation, energy flow density and $k_{\|}$ power spectrum distribution of the 3D ICRF antenna radiation under various conditions. The influence of induced currents on various components is also thoroughly examined. Additionally, a comparison of the coupling impedance was conducted between our simulations and the results obtained from EAST experiments, demonstrating a good agreement.

2. Simulation model

In this study, the geometric structure and mesh generation (as illustrated in Fig. 1) were performed using COMSOL software, which is then integrated into the 3DFEM-IA code to solve the electromagnetic field associated with the ICRF antenna. The simulation region is defined by a 3D Cartesian coordinate system, with the x, y, and z axes representing the toroidal, radial, and poloidal directions at the antenna location in the EAST tokamak. The dimensions of the simulation region are 1 m×0.6 m×1.6 m. Due to the open nature of the simulation area, ideal conductor boundary conditions are applied solely on the antenna window side. In contrast, a PML with a thickness of 0.1 m is implemented on the outermost layer in the remaining five directions to effectively absorb electromagnetic waves radiated by the antenna, thereby achieving the "single pass" model. The antenna structure employs a 3D reduced geometry of the current strap from the EAST ICRF antenna in B-window, consisting of a 2×2 arrangement of current straps oriented in both toroidal and poloidal directions. Each individual antenna current strap has dimensions of 0.344 m in length, 0.108 m in width, and 0.01 m in thickness. The distance from the surface of the antenna current strap closest to the plasma to the grounded end is 0.22 m. The metallic box has dimensions of 0.73 m×0.439 m×0.23 m, with a thickness of 0.01 m. Additionally, the thickness of the internal partition within the metallic box is 0.02 m.

Furthermore, it is important to note that the small structure of the Faraday cage would significantly increase the number of mesh elements and the complexity of the computations. As a result, the geometric structure of the Faraday shielding is excluded from the model. Nevertheless, constraint conditions are integrated into the calculation process, particularly in the Faraday shielding region. This effectively allows for assuming ideal Faraday shielding characteristics, which completely block the electric field $E_{\|}$ in the local area, parallel to the magnetic field.

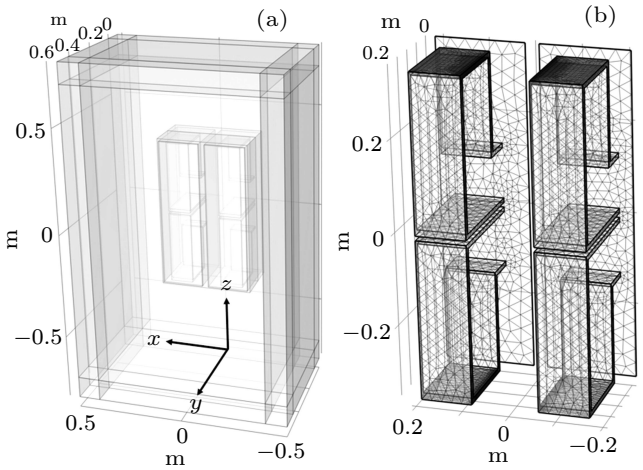


Fig. 1. (a) Schematic diagram of the simulation region, including antenna structure, electromagnetic field propagation area, and PML layer, (b) geometric structure and meshes of the four antenna current straps.

In the model, the cold plasma approximation of the dielectric tensor is employed to account for the anisotropic properties of the plasma. Given the relatively low temperature of the edge plasma, this approximation effectively characterizes the magnetized plasma near the antenna. The model uses the D (H) plasma with a minority fraction of 5% ($n_{\mathrm{H}} = 5\%\ n_{\mathrm{e}}$).[13] Under steady-state plasma conditions, the rate of change of plasma density in the toroidal and poloidal directions is significantly lower than that in the radial direction. Therefore, in the reduced model, plasma density is assumed to vary mainly in the radial direction, while densities in the toroidal and poloidal directions are uniform. The magnetic field is aligned with the toroidal direction, and its magnitude in the radial direction is described by the empirical formula $B_0 R_0 = BR$, where B_0 represents the magnetic field magnitude at the magnetic axis, and R_0 denotes the radial position of the magnetic axis. In this study, we reference the experimental parameters from the EAST device, specifically setting $B_0 = 2.42$ T and $R_0 = 1.85$ m. The radial position of the front surface of the antenna current strap close to the plasma side is $R = 2.39$ m. This corresponds to a transformation of the y-axis coordinate in the simulation as $y = 2.62\ \mathrm{m} - R$, allowing for the determination of the magnetic field at different radial positions.

In a magnetized plasma medium, we employ the wave equation for electric field distributions in the frequency domain:

$$\nabla \times \nabla \times \boldsymbol{E} - \omega_0^2 \mu \overleftrightarrow{\varepsilon} \boldsymbol{E} + \mathrm{i}\omega_0 \boldsymbol{J}_{\mathrm{ant}} = 0. \tag{1}$$

In this equation, $\omega_0 = 2\pi f_0$ represents the radio frequency, and all the work has been performed at $f_0 = 37$ MHz.[14,15] The $\boldsymbol{E}$ denotes the electric field, μ is the magnetic permeability tensor, $\overleftrightarrow{\varepsilon}$ is the dielectric tensor in the cold plasma approximation, i is the imaginary unit, and $\boldsymbol{J}_{\mathrm{ant}}$ refers to the current density at the antenna.

The dielectric tensor $\overleftrightarrow{\varepsilon}$ can be expressed as follows:

$$\overleftrightarrow{\varepsilon} = \overleftrightarrow{I} - \sum_{\alpha} \begin{pmatrix} \dfrac{\omega_\alpha^2}{\omega_0(\omega_0 + \mathrm{i}\nu_\alpha)} & 0 & 0 \\ 0 & \dfrac{(\omega_0 + \mathrm{i}\nu_\alpha)\omega_\alpha^2}{\omega_0\left[(\omega_0 + \mathrm{i}\nu_\alpha)^2 - \Omega_\alpha^2\right]} & \left(\dfrac{\Omega_\alpha}{\mathrm{i}\omega_0}\right)\dfrac{\omega_\alpha^2}{(\omega_0 + \mathrm{i}\nu_\alpha)^2 - \Omega_\alpha^2} \\ 0 & -\left(\dfrac{\Omega_\alpha}{\mathrm{i}\omega_0}\right)\dfrac{\omega_\alpha^2}{(\omega_0 + \mathrm{i}\nu_\alpha)^2 - \Omega_\alpha^2} & \dfrac{(\omega_0 + \mathrm{i}\nu_\alpha)\omega_\alpha^2}{\omega_0\left[(\omega_0 + \mathrm{i}\nu_\alpha)^2 - \Omega_\alpha^2\right]} \end{pmatrix}. \tag{2}$$

In this context, $\overleftrightarrow{I}$ represents the identity matrix, α denotes the label for various particle species, ω_α corresponds to the plasma oscillation frequency associated with species α, Ω_α indicates the cyclotron frequency, and ν_α signifies the collision frequency. In the vicinity of the ICRF antenna, the plasma collision frequency is significantly lower than the radio frequency. To simplify the model and focus on the plasma response to electromagnetic waves, this study neglects the collision processes near the antenna boundary, thus assuming $\nu_\alpha = 0$.

Within the PML, any electromagnetic wave entering experiences exponential decay in amplitude, thereby ensuring that no reflected waves return to the simulation region. The stretching function employed for the PML is based on the equations in Ref. [3]. In the frequency domain solution of the electric field wave equations, the dielectric tensor and permeability tensor within the PML are transformed following the method outlined in Ref. [16].

When solving the electric field wave equation, the surface current of the antenna serves as an excitation term that must be determined beforehand. This term is subsequently utilized as an input parameter in the finite element analysis of the electric field wave equation. In this study, we present a comparison between a uniform surface current distribution on the antenna strap and the self-consistent computation one using the method of moments (MOM).[17,18]

Measured coupling impedances under various plasma density scenarios derived from the EAST device are employed to compare the simulated results, thereby validating the reliability of the self-developed 3DFEM-IA code.

3. Simulation results and discussion

3.1. Propagation and coupling of electromagnetic fields in magnetized plasma

To facilitate a comparison with the performance of the actual ICRF antenna, the plasma density referenced in the simulation is derived from measurements obtained in the EAST device at three circumstances (i.e., n_{p1}, n_{p2}, n_{p3}), which are plotted in Fig. 2. It is important to note that although the range of the measured data is smaller than that of the simulation area, the density outside the measured region is corroborated by experimental data available in the literature.[15,19]

The scenario with uniform surface current density is first examined at various current phase configurations on the four antenna straps: $\begin{pmatrix} \pi & 0 \\ 0 & \pi \end{pmatrix}\begin{pmatrix} \pi/2 & 0 \\ 3\pi/2 & \pi \end{pmatrix}\begin{pmatrix} 0 & 0 \\ \pi & \pi \end{pmatrix}$. For simplicity, the four phase configurations mentioned above will be represented by $(\pi\ 0; 0\ \pi)$, $(\pi/2\ 0; 3\pi/2\ \pi)$, and $(0\ 0; \pi\ \pi)$ in the following text.

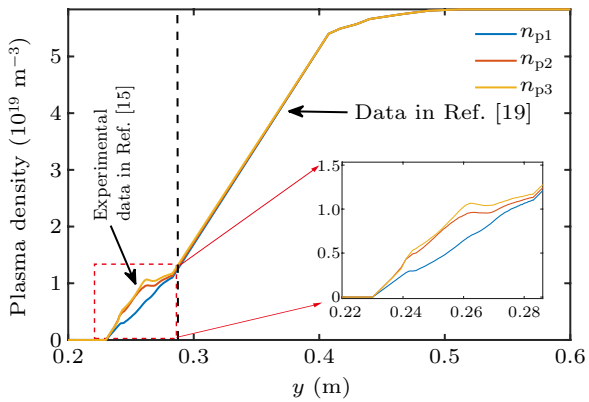


Fig. 2. Radial distributions of plasma density around the antenna measured in the EAST device (n_{p1}, n_{p2}, n_{p3}). The data were derived from Refs. [15,19].

Figure 3 illustrates the 3D distribution of the surface current density on the antenna straps. The electric field distribution excited by different antenna phases was accordingly calculated, including the E_y radial field, E_z poloidal field, and the E_x toroidal field (also referred to as $E_{\parallel}$ field) at a distance of 35 mm in front of the antenna. Given the minimal differences across various plasma densities, only the data at plasma density n_{p3} is presented, as illustrated in Figs. 4 and 5.

The propagation of electromagnetic waves (fast waves) generated by the RF antenna into the plasma is illustrated by

the periodic spatial distribution of the electric fields, as shown in Fig. 4. Figure 5 demonstrates that, despite the implementation of ideal Faraday shielding in the simulation to eliminate parallel electric fields at the Faraday plane, weak parallel electric fields were nevertheless generated near the plasma side and outside the antenna box. The E_x field may induce substantial radio frequency sheath potentials on nearby components, such as the limiter, metal box, and Faraday shield, which can subsequently result in significant sputtering impurities, and further affect the power deposition in the core plasma region. When the phase of the radio frequency antenna is altered, the spatial distribution of the emitted electric field exhibits significant variations. Specifically, when the phase differences of adjacent antenna straps in the toroidal direction are π $\pi/2$ and 0 (i.e., the three columns in Fig. 4), the radiating fast wave electric field exhibits anti-symmetric, asymmetric, and symmetric distributions in the toroidal direction, respectively. Conversely, under the same phase conditions, the $E_{\|}$ field exhibits symmetric, asymmetric, and anti-symmetric distributions in the toroidal direction.

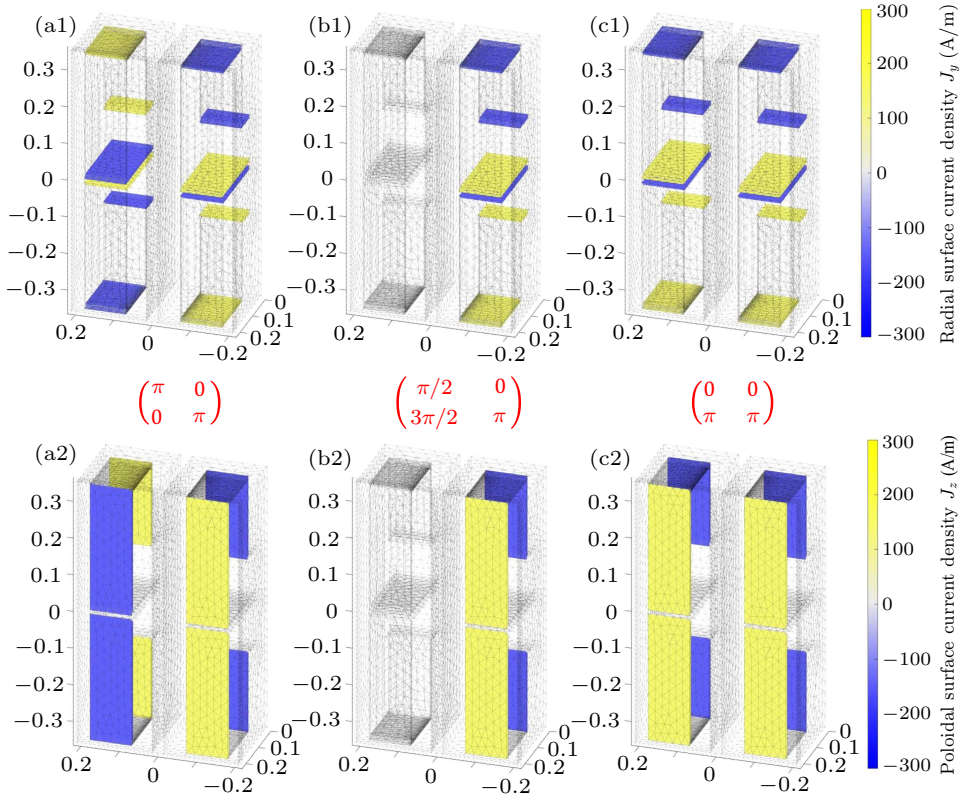


Fig. 3. Distribution of the uniform surface current density on the antenna current strap for 3 antenna phase configurations: (a) $(\pi\,0;0\,\pi)$ phases, (b) $(\pi/2\,0;3\pi/2\,\pi)$ phases, (c) $(0\,\pi;0\,\pi)$ phases. First row: radial surface current density J_y; second row: poloidal surface current density J_z.

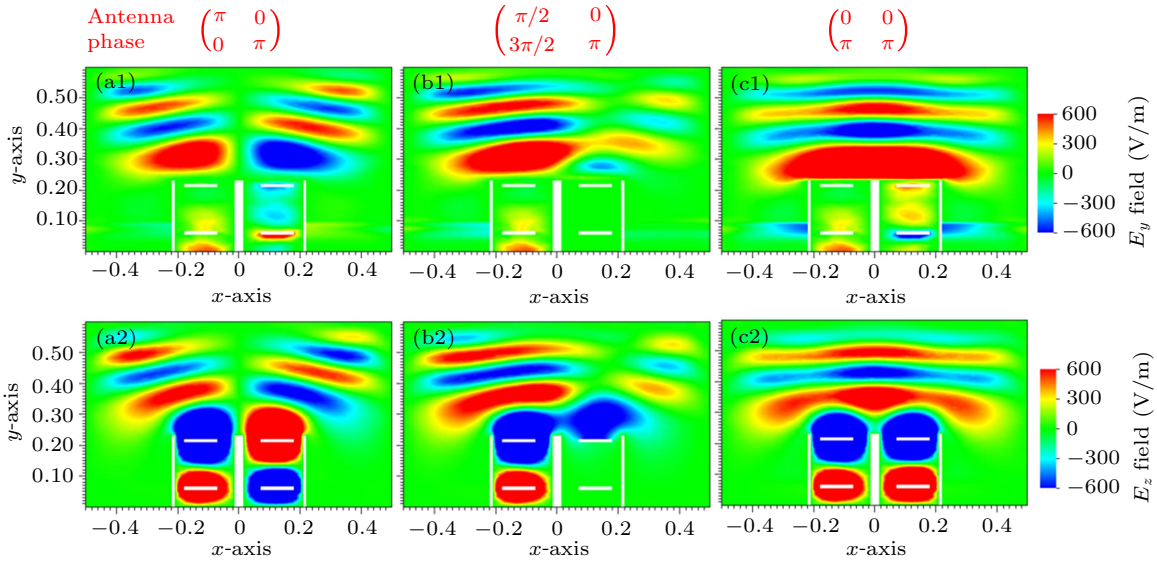


Fig. 4. Spatial distribution of the real parts of the E_y field and E_z field excited by the uniform current density on the antenna surface at a position of 0.2 m in the poloidal direction under 3 phases.

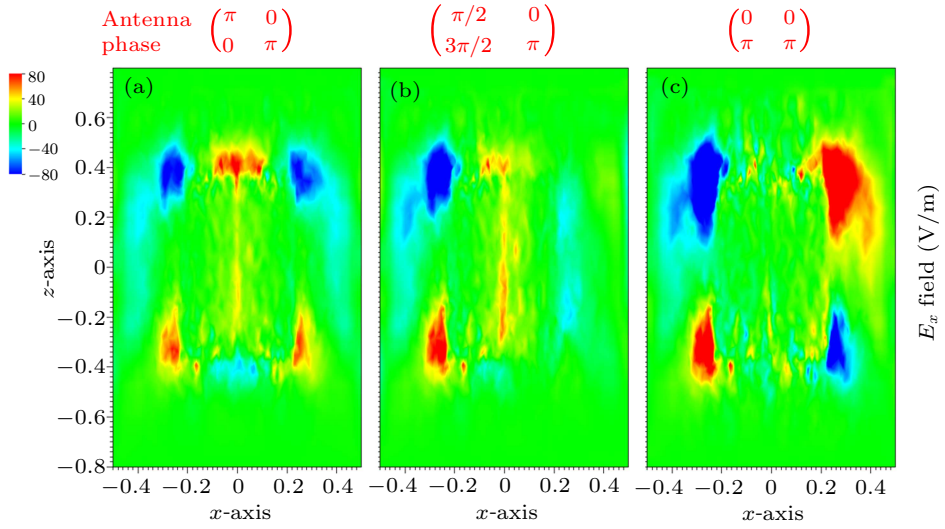


Fig. 5. Spatial distribution of the real parts of the E_x field excited by the uniform current density on the antenna surface at a distance of 35 mm in front of the antenna under 3 phases.

To gain a deeper understanding of the coupling characteristics between the antenna and the edge plasma, it is essential to calculate the electromagnetic energy flow density vector, given by $S = \text{real}(\text{conj}(E) \times B)/2$, where $\text{conj}(E)$ represents the complex conjugate of the electric field $\boldsymbol{E}$. This calculation yields the distributions of the time-averaged energy flow density components S_x, S_y, as illustrated in Fig. 6. Fast waves primarily propagate in the x and y directions, with no propagation occurring in the z direction. Consequently, the energy flow density vector in the z direction can be disregarded. Different antenna phases result in variant directions of energy propagation for the electromagnetic waves emitted by the antenna, which correspond to distinct radiation patterns. Specific differences can be identified by comparing the power spectra derived from subsequent calculations.

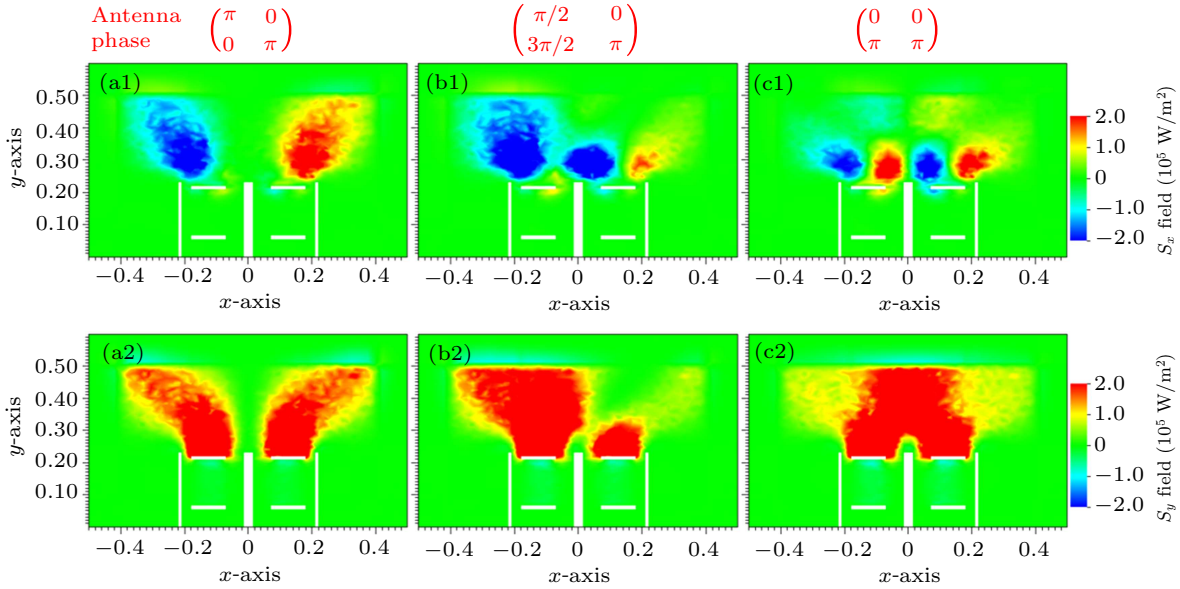


Fig. 6. Spatial distribution of the time-averaged energy flow density vectors S_x, S_y of the radiating electromagnetic field at a position of 0.2 m in the poloidal direction under 3 phases.

The total coupling power is derived from the surface integral of the energy flow density vector

$$P = \int_{\Gamma} S \mathrm{d}\Gamma. \tag{3}$$

Here, Γ is the surface around the antenna. In our simulation, we take the inner surface of the PML and the boundary of the antenna sidewall as the integration surface Γ. After determining the total coupling power, the coupling impedance can be calculated using the following formula:[20]

$$R_{\mathrm{c}} = \frac{2P}{|I|^2}. \tag{4}$$

Here, $|I|$ denotes the total current of the antenna. Figure 7 illustrates the coupling impedances associated with various antenna phases, calculated under three distinct plasma density distributions.

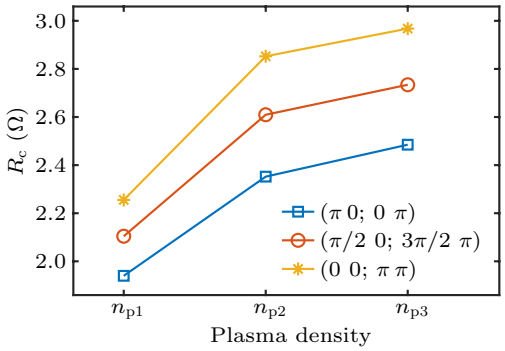


Fig. 7. The coupling impedances calculated under variant plasma densities and antenna phases, with a uniform current density distribution.

The data indicate that the coupling impedance attains its maximum at a constant plasma density when the phase difference of the antenna in the toroidal direction is zero. Additionally, for a fixed antenna phase, the coupling impedance is maximized at the plasma density distribution of n_{p3}. This suggests that an increase in the edge plasma density also leads to an increase in coupling impedance. As the plasma density increases, the distance between the fast wave cutoff layer and the antenna decreases, resulting in reduced attenuation of fast waves in that region and allowing more power to be injected into the plasma. By increasing the plasma density in front of the antenna (such as through local gas puffing) or by adjusting the plasma edge position, for example, by changing the radial position of the limiter to bring it closer to the antenna surface, both the coupling impedance and coupling power of the antenna can be effectively enhanced. However, decreasing the distance to the plasma may exacerbate sputtering due to more ion bombardment, potentially increasing impurity concentration in the plasma core. Therefore, the effective operation necessitates a careful balance between enhanced coupling impedance and the risk of sputtering damage to the antenna.

To further evaluate additional coupling parameters, a Fourier transform is applied to the electromagnetic field at n_{p3} density scenario, yielding the $k_{\|}$ power spectrum depicted in Fig. 8.

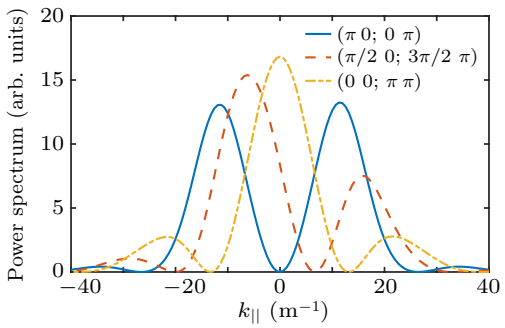


Fig. 8. The $k_{\|}$ power spectrum emitting under 3 antenna phases with uniform current density on the antenna surface.

The peak value of the excited RF wave is observed at $k_{\|} = 12$ m^{-1} when the toroidal phase difference of the RF antenna is π (π 0;0 π). This result is consistent with both the simulations[11] and experimental data[15] from the ICRF antenna B window on the EAST device, confirming the accuracy of our simulation. Additionally, the peak value reaches its maximum when the toroidal phase difference is $\pi/2$, corresponding to a specific phase configuration ($\pi/2$ 0;3$\pi/2$ π).

When the toroidal phase difference is 0 or $\pi/2$, power deposition occurs near $k_{\|} = 0$, indicating that considerable electromagnetic waves radiated by the antenna propagate along radial direction (i.e., the direction perpendicular to magnetic field lines). These conditions have been demonstrated to result in significantly low heating efficiency in the core plasma region.[21] The waves can easily penetrate the core of the plasma, leading to multiple reflections within the device, which partially heats the edge plasma. This phenomenon intensifies the interaction between the plasma and the vessel walls, increases sputtering, exacerbates radiation losses, and ultimately reduces overall heating efficiency. Consequently, the π phase is often selected for plasma heating in experiments due to its superior heating efficiency, even though the calculated coupling impedance is minimized (as shown in Fig. 7).

3.2. Antenna surface current distribution and coupling characteristics

In a realistic ICRF antenna, induced currents occur on both the antenna current strap and the surface of the metal box. This phenomenon causes the actual current density distribution to deviate from the simplified assumption of uniformity. To better reflect the simulation conditions, we employed the method of moments (MOM) to obtain the surface current density distribution, as shown in Fig. 9.

It can be observed that the current density is primarily concentrated on the two sides of the antenna current strap, while a reverse current distribution is also excited on the adjacent metallic box. Using this current density distribution as input, the finite element method was utilized to solve the electromagnetic wave equation. The electromagnetic field corresponding to the non-uniform current distribution is illustrated in Fig. 10 (only the simulation results for the n_{p3} density distribution are presented).

Upon comparing Figs. 10 and 4, as well as Figs. 11 and 5, it is evident that the electromagnetic field amplitude produced under a non-uniform current density distribution is slightly lower than that in the uniform one. This difference primarily arises from the induced currents generated by the antennas and the metallic box, which induce opposite currents that diminish the originally radiating electromagnetic field. The energy flow density vectors for three antenna phases were calculated, and the corresponding coupling impedances are presented in Fig. 12.

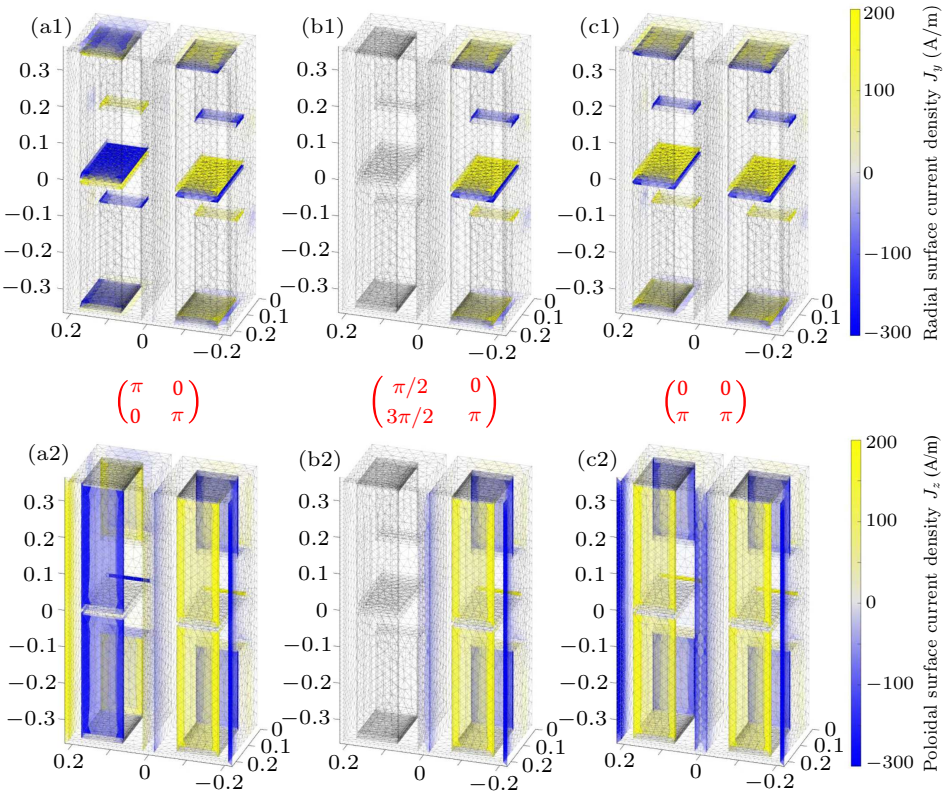


Fig. 9. Distribution of the surface current density on the antenna current strap with MOM for 3 antenna phase configurations: (a) $(\pi\ 0;0\ \pi)$ phases, (b) $(\pi/2\ 0;3\pi/2\ \pi)$ phases, (c) $(0\ \pi;0\ \pi)$ phases. First row: radial surface current density J_y. Second row: poloidal surface current density J_z.

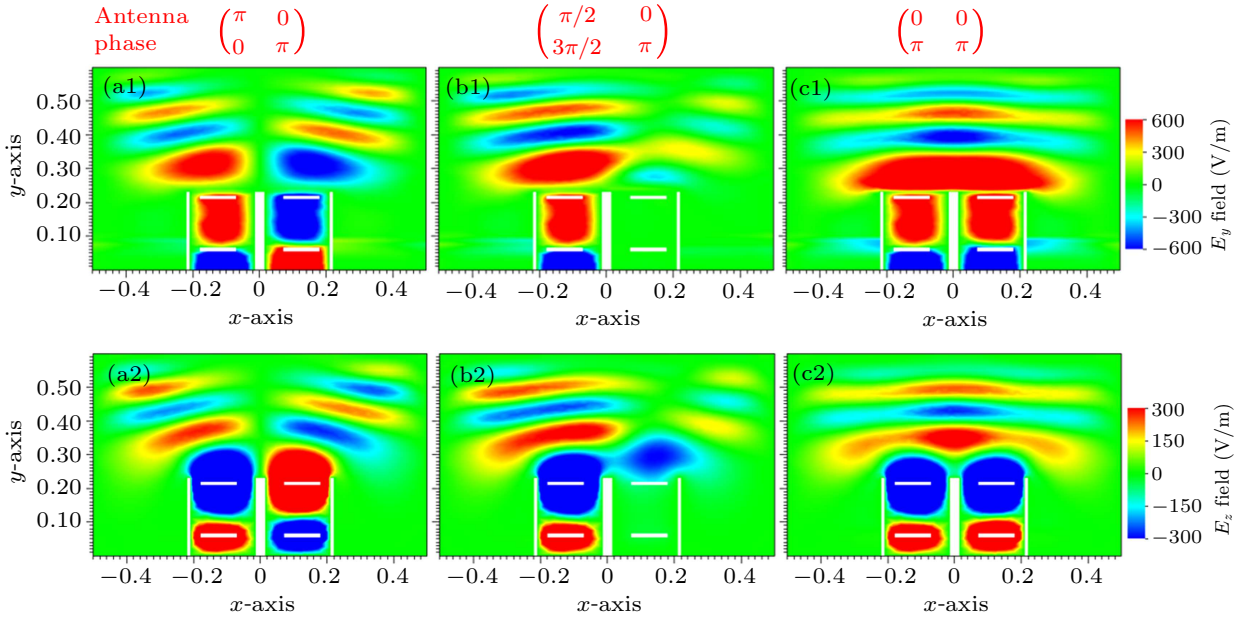


Fig. 10. Spatial distribution of the real parts of the E_y field and E_z field excited by the non-uniform current density on the antenna surface at a position of 0.2 m in the poloidal direction under 3 phases.

A comparison between Figs. 7 and 12 reveals that the trends in coupling impedance for a non-uniform current density distribution are consistent with those obtained from a uniform current density distribution. In both scenarios, the coupling impedance is higher at the $(0\ 0;\pi\ \pi)$ phase and at elevated edge plasma densities. However, at identical plasma density and antenna phase parameters, the coupling impedance calculated with a uniform current density distribution is always higher, suggesting that the power coupled into the plasma is greater. The primary reason for this effect is that the induced currents generated on the antenna straps and the metal box diminish the electromagnetic field radiated by the antenna. To mitigate this issue, various antenna configurations, including array antennas, can be employed while adjusting phase and current amplitude parameters to minimize the induced current on the metal box. Furthermore, increasing

the distance between the antenna strap and the metal box wall or applying a coating to the box may further diminish the intensity of the induced current. The overall trend of coupling impedance observed in the simulations for a non-uniform current density distribution aligns with the experimental findings. Figure 13 illustrates further analysis of the parallel power spectrum, which is derived by applying a Fourier transform to the electromagnetic fields simulated under the specified density distribution of n_{p3}.

By comparing the $k_{\parallel}$ power spectra derived from uniform current density in Fig. 8 and non-uniform current density in Fig. 13, it is evident that the total coupled power decreases under non-uniform conditions. This reduction is indicated by the lower peak heights in the $k_{\parallel}$ power spectrum across the 3 antenna phase configurations. Notably, when the toroidal phase difference of the antenna is 0 (0 0; π π), the peak amplitude experiences the most significant reduction compared to the uniform case, becoming the smallest among the three toroidal phase differences. However, the overall distribution of the power spectrum remains relatively unchanged.

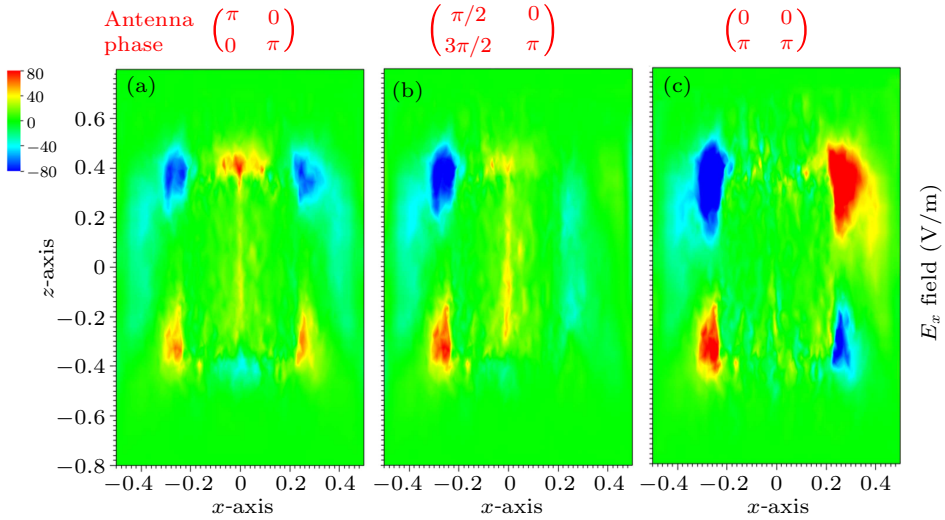


Fig. 11. Spatial distribution of the real parts of the E_x field excited by the non-uniform current density on the antenna surface at a distance of 35 mm in front of the antenna under 3 phases.

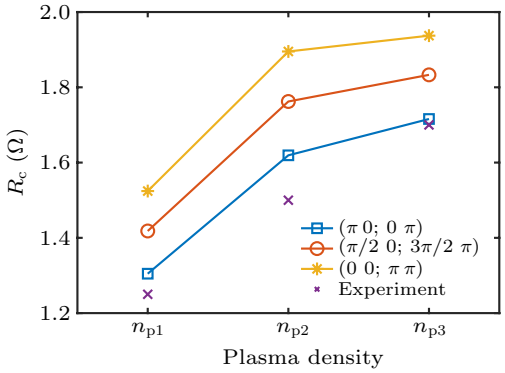


Fig. 12. The coupling impedances calculated under variant plasma densities and antenna phases with a non-uniform current density distribution, as well as the experimentally measured antenna coupling impedances[15] for the EAST device at the corresponding plasma densities.

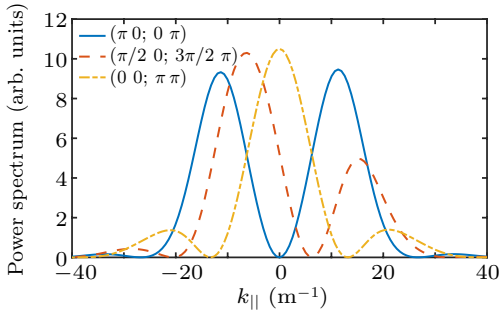


Fig. 13. The $k_{\parallel}$ power spectrum emitting under 3 antenna phases with non-uniform current density on the antenna surface.

4. Conclusion

This work investigates the characteristics of electromagnetic wave propagation and coupling between the ICRF antenna and the edge plasma in a tokamak. Utilizing a self-developed 3DFEM-IA code based on finite element method to solve the electric field wave equations, systematic simulations were conducted to assess the coupling characteristics of the ICRF antenna under variant antenna phases and plasma densities. The results indicate significant differences in both the propagation characteristics of the electric field and the energy flow density under different conditions. Furthermore, a significant difference in coupling power is noted between uniform and non-uniform distributions of surface current density on the antenna straps, the latter resulting in reduced coupling power. This non-uniform surface current is typically observed on the antenna straps due to the influence of induced currents at high frequencies. Additionally, the coupling impedance is observed to increase with background plasma density, which reduces the distance from the cutoff layer to the antenna. This impedance reaches its highest value in the case where there is no toroidal phase difference between the antenna straps, which aligns well with experimental data. This research enhances our understanding of the plasma heating process and

provides a theoretical framework, as well as technical guidance, for improving the heating efficiency of ICRF technology in tokamaks.

Acknowledgements

Project supported by the National MCF Energy Research and Development Program (Grant No. 2022YFE03190100), the National Natural Science Foundation of China (Grant Nos. 12422513, 12105035, and U21A20438), and the Xiaomi Young Talents Program.

References

[1] Porkolab M, Bécoulet A, Bonoli P T, Gormezano C, Koch R, Majeski R J, Messiaen A, Noterdaeme J M, Petty C, Pinsker R, Start D and Wilson R 1998 *Plasma Phys. Control. Fusion* **40** A35

[2] Yin L, Yang C, Gong X Y, Lu X Q, Du D and Chen Y 2017 *Phys. Plasmas* **24** 102502

[3] Yang H, Zhang X J, Qin C M, Zhao Y P, Yuan S, Mao Y Z, Yang X, Li M H, Urbanczyk G, Wang M, Wang X J, Xu H D, Ding B J, Li Y C, Xu G S, Hu L Q, Ai L and Guo Y Y 2021 *Nucl. Fusion* **61** 035001

[4] Clairet F, Colas L, Heuraux S and Lombard G 2004 *Plasma Phys. Control. Fusion* **46** 1567

[5] Jacquet P, Bobkov V, Mayoral M L, Monakhov I, Noterdaeme J M, Scarabosio A, Stepanov I, Vrancken M, Wolfrum E and the ASDEX Upgrade Team 2012 *Nucl. Fusion* **52** 042002

[6] Carter M D, Wang C Y, Hogan J T, Harris J H, Hoffman D J, Rasmussen D A, Ryan P M, Stallings D S, Batchelor D B, Beaumont B, Hutter T and Saoutic B 1996 *AIP Conf. Proc.* **355** 364

[7] Milanesio D, Helou W, Polli V, Durodié F, Lamalle P, Louche F and Zhang W 2023 *AIP Conf. Proc.* **2984** 060008

[8] Jacquot J, Colas L, Clairet F, Goniche M, Heuraux S, Hillairet J, Lombard G and Milanesio D 2013 *Plasma Phys. Control. Fusion* **55** 115004

[9] Usoltceva M, Tierens W, Kostic A, Noterdaeme J M, Ochoukov R and Zhang W 2020 *AIP Conf. Proc.* **2254** 050003

[10] Tierens W, Milanesio D, Urbanczyk G, Helou W, Bobkov V, Noterdaeme J M, Colas L, Maggiora R, the ASDEX Upgrade Team and the EUROfusion MST1 Team 2019 *Nucl. Fusion* **59** 046001

[11] Qin C M, Zhang X J, Zhao Y P, Wan B N, Braun F, Wang L, Yang Q X, Yuan S, Cheng Y and ICRF team on EAST 2015 *Plasma Sci. Technol.* **17** 167

[12] Yang H, Wu C F, Dong S, Zhao Y P, Zhang X J and Shang L 2016 *Nucl. Sci. Tech.* **27** 46

[13] Zhong G Q, Cao H R, Hu L Q, Zhou R J, Xiao M, Li K, Pu N, Huang J, Liu G Z, Lin S Y, Lyu B, Liu H Q, Zhang X J and EAST Team 2016 *Plasma Phys. Control. Fusion* **58** 075013

[14] Zhou L, Beck W K, Koert P, Doody J, Vieira R F, Wukitch S J, Granetz R S, Irby J H, Yang Q X, Qin C M, Zhang X J and Zhao Y P 2016 *IEEE Trans. Plasma Sci.* **44** 1731

[15] Zhang W, Liu L N, Zhang X J, Qin X M, Yang H and the EAST Team 2024 *Nucl. Fusion* **64** 096011

[16] Colas L, Jacquot J, Hillairet J, Helou W, Tierens W, Heuraux S, Faudot E, Lu L and Urbanczyk G 2019 *Journal of Computational Physics* **389** 94

[17] Harrington R F 1968 *Field Computation by Moment Methods. Macmillan* (IEEE Operations Center)

[18] Rao S M, Wilton D R and Glisson A W 1982 *IEEE Trans. Anten. Propag.* **AP-30** 409

[19] Li J H, Yang Q X, Song Y T, Yu C, Chen S L, Xu H and Du D 2021 *J. Nucl. Sci. Technol.* **58** 837

[20] Bhatnagar V P, Koch R, Messiaen A M and Weynants R R 1982 *Nucl. Fusion* **22** 280

[21] Lerche E, Bobkov V, Jacquet P, Mayoraf M L, Messiaen A, Monakhov I, Ongena J, Telesca G, Van Eester D, Weynants R R and JET-EFDA Contributors 2009 *AIP Conf. Proc.* **1187** 93